

KERNEL PHASE IN FIZEAU INTERFEROMETRY

FRANTZ MARTINACHE
Subaru Telescope, Hilo, HI, USA

Received 2010 June 20; accepted 2010 September 16; published 2010 November 2

ABSTRACT

The detection of high contrast companions at small angular separation appears feasible in conventional direct images using the self-calibration properties of interferometric observable quantities. The friendly notion of closure phase, which is key to the recent observational successes of non-redundant aperture masking interferometry used with adaptive optics, appears to be one example of a wide family of observable quantities that are not contaminated by phase noise. In the high-Strehl regime, soon to be available thanks to the coming generation of extreme adaptive optics systems on ground-based telescopes, and already available from space, closure phase like information can be extracted from any direct image, even taken with a redundant aperture. These new phase-noise immune observable quantities, called kernel phases, are determined a priori from the knowledge of the geometry of the pupil only. Re-analysis of archive data acquired with the *Hubble Space Telescope* NICMOS instrument using this new kernel-phase algorithm demonstrates the power of the method as it clearly detects and locates with milliarsecond precision a known companion to a star at angular separation less than the diffraction limit.

Key words: binaries: close – methods: data analysis – stars: low-mass – techniques: high angular resolution – techniques: image processing – techniques: interferometric

1. PHASE IN THE FOURIER PLANE

Only two parameters essentially determine whether a source is detectable during an observation: its brightness at the wavelength λ of interest and the angular resolution necessary to separate the source or feature from its direct environment. The angular resolution is ultimately constrained by the diffraction of the telescope, and astronomers usually follow the rule of thumb known as the Rayleigh criterion, stating that to be resolved, two sources need to be separated by $1.22\lambda/D$, where D is the diameter of the telescope used, to design their observations.

The development of optical interferometry has however made this criterion obsolete: thanks to the exquisite level of calibration it permits, interferometry indeed makes it possible to detect sources or constrain the extent of features around objects at separations significantly smaller than the diffraction limit. Even at the scale of one single telescope, the results obtained with the technique known as non-redundant masking (NRM) interferometry, first, seeing-limited (Haniff et al. 1987; Readhead et al. 1988) and more recently used with adaptive optics (AO) systems (Tuthill et al. 2000, 2006; Lloyd et al. 2006; Ireland et al. 2008; Kraus et al. 2008; Martinache et al. 2009) demonstrate the relevance of this technique for the detection of structures at small angular separation, that would not be accessible from conventional AO images (Rajagopal et al. 2004).

Even if it only uses one single telescope in order to reach this level of resolution, one however needs to accept that the familiar product called “image” may not necessarily constitute the best final data product. Instead, when interested in high-angular resolution properties of partially resolved objects, it is convenient to derive information not from the image itself, but from its Fourier-transform counterpart. This information, known as complex visibility, is extracted from the Fourier plane, calibrated and then tested against a model of the observed object.

In optical interferometry, this approach is often mandatory: the paucity of apertures ($N \sim 2\text{--}5$) and baselines make the content of a direct (Fizeau) image of limited value. Information-rich images can be reconstructed after extraction of the complex visibility function from the (u, v) -plane, but only with a

large ($N > 10$) number of apertures as in radio interferometry, or after using image synthesis. The optical image reconstruction known as pupil densification that is used in hypertelescopes (Labeyrie 1996) does provide an alternative, but again, only becomes compelling if a large number of apertures are used (Labeyrie et al. 2008). But even when an image can be reconstructed from optical interferometry measurements, e.g., the images of the binary Capella by Baldwin et al. (1996), the intensity map of the surface of Altair by Monnier et al. (2007) or the spectacular images of the disk eclipsing ϵ Aurigae (Kloppenborg et al. 2010), quantitative characteristics of the sources can only be deduced from the fit of the interferometric data by parametric models. In the case of a marginally resolved binary star, precise measurements of angular separation, orientation and contrast, with confidence intervals, deduced from a model fit of complex visibilities carry much more scientific value than an image of “blurry blobs.”

Visibilities in the Fourier plane are complex numbers, whose amplitude and phase are usually considered separately. This paper focuses on the treatment of the phase and ignores the amplitude. In general, the power contained at given spatial frequency is the result of the coherent sum of R random phasors, with R being a scalar coding the redundancy of the spatial frequency. In the presence of residual optical path differences (OPDs), this coherent sum of R random phasors loses the phase information and results in the formation of speckles in seeing-limited images with a visible/IR telescope. NRM interferometry solves this problem, by discarding light with a pupil mask designed so that each baseline is unique ($R = 1$), which makes the extraction of the phase possible.

The phases alone, being corrupted by residual OPDs, are of restricted interest. It is however possible to combine them to form what is known as closure phase (Jennison 1958), that is the sum of three phases measured by baselines forming a closed triangle. This remarkable interferometric quantity (cf. the introduction to closure phase by Monnier 2000) exhibits a compelling property: it rejects all residual pupil-plane phase errors. Moreover, because it is determined from the analysis of the final science detector and not on a separate arm wavefront

sensor, it is also immune to non-common path errors between the wavefront sensor and the science camera.

Once extracted and calibrated, the closure phases can then be compared to a parametric model, for instance of a binary star, to confirm or infirm the presence of a companion around a given source, while uncertainties provide contrast detection (i.e., sensitivity) limits. This approach was successfully used by Lloyd et al. (2006), Martinache et al. (2007), Ireland et al. (2008), Kraus et al. (2008), and Martinache et al. (2009), who typically report sensitivity of 5–6 mag in the near-infrared at separations ranging from 0.5 to $4 \lambda/D$.

This paper aims at generalizing the notion of closure phase, and shows that closure phase like quantities, i.e., sharing the same property of independence to pupil-plane phase errors, can be constructed even in the case of redundant apertures.

2. KERNEL PHASE

2.1. Linear Model

Whether contiguous (i.e., single dish) or not (i.e., interferometric), the two-dimensional pupil of an imaging system can be discretized into a finite collection of N elementary sub-apertures. One of these elementary sub-apertures taken as zero-phase reference, the pupil-plane phase of a coherent point-like light source can be written as an $(N - 1)$ -component vector φ . Given that the image, or interferogram, of this source is sufficiently sampled, then in the Fourier plane (a.k.a. (u, v) -plane in interferometry) one will be able to sample up to M phases, where M is a function of the pupil geometry only. For a non-redundant array made of N elementary sub-apertures, the number of sampled (u, v) phases is maximum $M = \binom{N}{2}$. The same number of sub-apertures organized in a redundant array, for instance following a regular grid, produces significantly less distinct (u, v) sample points as each point receives the contribution of several pairs of sub-apertures.

In most cases, since each point receives the sum of several random phasors, both phase and amplitude are lost and cannot be simply retrieved: this results in the formation of speckles. However, if the Strehl is high enough, the complex amplitude associated with the instrumental phase in one point of the pupil, φ_k , can be approximated by $e^{i\varphi_k} \approx 1 + i\varphi_k$. Direct application of the approach is therefore for now restricted to space-borne diffraction-limited optical and mid-IR telescopes like *HST* (cf. Section 3), but should also prove relevant to the upcoming generation of extreme AO systems.

Given that the proposed approximation holds, while observing a point source, the unknown (instrumental) phase distribution in the pupil φ can be related to the phases Φ measured in the Fourier plane with a single linear operator. To build an intuitive understanding of this relation, let us consider the following scenarios.

1. If the phase is constant across the entire pupil, then none of the baselines formed by any pair of elementary sub-apertures does record a phase difference, and the phase in the Fourier plane is zero everywhere.
2. If a phase offset δ_ϕ is added to one single sub-aperture, then each baseline involving this aperture records a phase difference, which is exactly $\pm\delta_\phi$. Figure 1 represents several such scenarios.
3. If the pupil-plane phase vector φ is completely random, each of the M samples in the Fourier plane is then the average of R phase differences on the pupil, where R is the redundancy of the considered baseline.

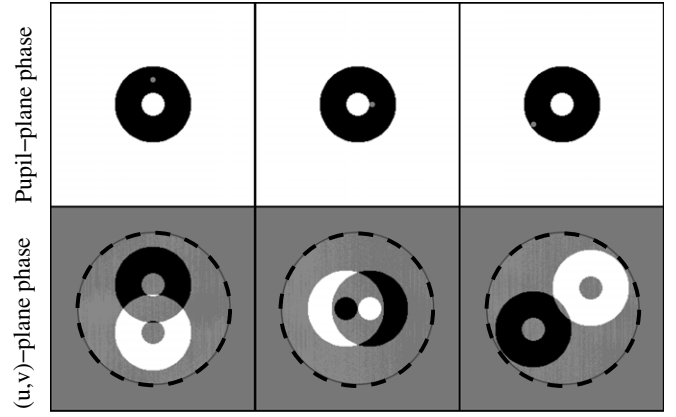


Figure 1. Iterative process for the determination of the transfer matrix \mathbf{A} . The top row shows the sub-aperture of the full two-dimensional pupil (circular aperture with 30% central obscuration), where a phase offset is applied (three cases are represented). The bottom row shows the resulting distribution of phase in the Fourier plane. The overlaid dashed-line circle in the bottom row marks the cutoff spatial frequency of the transfer function.

To reproduce this behavior, the following linear model will be used:

$$\Phi = \mathbf{R}^{-1} \cdot \mathbf{A} \cdot \varphi, \quad (1)$$

where Φ represents the M -component Fourier plane phase vector, \mathbf{R} an $M \times M$ diagonal matrix whose diagonal elements code the redundancy of the baselines, and \mathbf{A} represents an $M \times (N - 1)$ transfer matrix, whose properties form the core of the discussion of this work. To be complete, the model should also include the phase information intrinsic to the observed source, represented by the term Φ_O that simply adds on top of the instrumental phase. One can then multiply both sides of the equation by the matrix \mathbf{R} so that it becomes

$$\mathbf{R} \cdot \Phi = \mathbf{A} \cdot \varphi + \mathbf{R} \cdot \Phi_O. \quad (2)$$

While \mathbf{R} and \mathbf{A} could have been merged into one single operator, they are intentionally kept distinct. The rationale for this choice is so that the left-hand side of Equation (2), i.e., the measurements, can be acquired by reading directly the imaginary part of the complex visibility. Given that the next (quadratic) term in the Taylor expansion of $e^{i\varphi}$ being real, this makes the approximation valid to the third order in phase. This also makes \mathbf{A} of striking aspect as it is then exclusively filled with values 0, 1, or -1 .

If the matrix \mathbf{A} were invertible, then the analysis of one unique focal plane image of a single star (case corresponding to Equation (1)) would be sufficient to determine the instrumental phase φ as seen from the detector, and drive an AO system and/or delay lines. Except for the special case of a non-redundant aperture, the problem is however known to be degenerate, despite the larger number of measures than unknowns ($M > N - 1$).¹

As demonstrated by the successes of NRM interferometry, a complete characterization of the wavefront is not essential if one can determine observable quantities that are pupil-phase independent. The closure relations used in interferometry can be related to the operator \mathbf{A} : these relations are simply linear combinations (modeled by an operator \mathbf{K}) of rows of \mathbf{A} that

¹ The use of this model for wavefront sensing purposes will be the object of another paper.

produce 0, forming something known as the left null space of \mathbf{A} :

$$\mathbf{K} \cdot \mathbf{A} = \mathbf{0}. \quad (3)$$

For a non-redundant array, each closure relation will fill a row of \mathbf{K} with mostly zeroes, except in three positions corresponding to the baselines forming a closing triangle, that will contain 1 or -1 . These relations are however not the only possible ones, and less trivial combinations, involving more than three rows at a time, can be constructed. The total number of independent relations however remains unchanged and is only imposed by the geometry of the array.

Although not impossible, finding the operator \mathbf{K} “by hand” (i.e., finding a basis for the left null space of \mathbf{A}) for a redundant aperture is a tedious task, as the matrix \mathbf{A} can get quite large. A very efficient way to do this is to calculate the singular value decomposition (SVD) of \mathbf{A}^T . The SVD algorithm (Press et al. 2002) allows us to decompose the now $(N - 1) \times M$ matrix \mathbf{A}^T as the product of an $(N - 1) \times M$ column-orthogonal matrix \mathbf{U} , an $M \times M$ diagonal matrix \mathbf{W} with positive or zero elements (the so-called singular values), and the transpose of an $M \times M$ orthogonal matrix \mathbf{V} :

$$\mathbf{A}^T = \mathbf{U} \cdot \mathbf{W} \cdot \mathbf{V}^T. \quad (4)$$

One relevant property of the SVD is that it explicitly constructs orthonormal bases for both the null space and the range of the matrix \mathbf{A}^T . Of particular interest here are the columns of \mathbf{V} that correspond to singular values equal to zero: these vectors form an orthonormal base for the null space, also referred to as Kernel of \mathbf{A}^T , that is exactly what is needed to fill in the rows of \mathbf{K} .

If the observed target is not perfectly symmetric, and exhibits actual phase information (i.e., $\Phi_O \neq 0$, see for instance Monnier 2000), Equation (2) is required. Multiplying it with the left side operator \mathbf{K} leads to a new series of new phase-like quantities that are not contaminated by instrumental phase, generalizing the notion of closure phase (Baldwin et al. 1986) on which NRM interferometry from the ground (Tuthill et al. 2000) and from space (Sivaramakrishnan et al. 2009) entirely rely.

While not as immediately tangible as the notion of closure phase, this proposed generalization, hereafter referred to as kernel phase (or Ker-phase) since it relates to the kernel of the matrix \mathbf{A}^T , exhibits a unique advantage over the classical closure phase: it is not restricted to non-redundant apertures and makes it possible to extract phase-residual immune information from images acquired from telescopes of arbitrary pupil geometry.

This has some obvious advantages over the restrictive non-redundant case:

1. Throughput: non-redundant aperture masks exhibit a typical 5%–15% throughput (Martinache et al. 2007), and photon noise of the companion one tries to detect may be the dominant source of noise. Given that it benefits from the same phase-noise canceling properties as closure phase, for a given readout noise and exposure time, kernel phase on an unmasked aperture offers an immediate boost in sensitivity (or dynamic range) on faint sources.
2. Number of observable quantities: a common non-redundant aperture mask design exhibits nine sub-apertures, therefore forming $\binom{9}{2} = 36$ baselines and $\binom{8}{2} = 28$ independent closure phases (Monnier 2000). More independent kernel phases can be extracted from the Fourier transform of a full-aperture image, which will provide a better characterization of the target.

Another incidental advantage is that, being a product of the SVD, all the kernel-phase relations contained in \mathbf{K} form an orthonormal basis, and therefore do not introduce correlation in the data. A consequence is that manipulating Ker-phases does not require keeping track of the covariance matrix used for closure phases in masking interferometry, which simplifies their interpretation.

2.2. Calibration

In discretizing the pupil into a finite number of sub-apertures, one important assumption is made: the phase (or more generally, the complex amplitude of the electric field) is assumed to be uniform within each sub-aperture. Yet even for a space-borne telescope, in the absence of atmosphere, this is only an idealization as small-scale structures, like polishing imperfections of the primary mirror for instance, will impact, to some extent, the value of the Ker-phases. This issue is not proper to Ker-phases and also affects closure phases. Thus, unless perfect (i.e., single mode) spatial filtering is performed within each sub-aperture of a non-redundant array, the closure phase on a point source is not exactly be zero.

This effect can somewhat be mitigated by subtracting from the Ker-phases of a science target, the Ker-phase signal measured on a point source observed in identical conditions. NRM interferometry results reported in Martinache et al. (2009), for instance, make extensive use of this kind of calibration: from the ground, this approach is very powerful as it makes it possible to calibrate other sources of systematic errors like the effect of broadband filters which smear out the Fourier plane and differential atmospheric refraction. From space, this may not be as essential depending on the science goal: if the Ker-phases obtained on a binary system are non-calibrated, then they will simply contain a systematic error term that will limit the achievable contrast.

3. KERNEL-PHASE ANALYSIS OF *HST*/NICMOS DATA

While the kernel-phase approach may prove difficult to apply to ground-based observations until extreme AO become available, it can readily be applied to diffraction-limited observations made from space. It is tested here on a series of non-coronagraphic narrowband images acquired with the Near-Infrared Camera and Multiobject Spectrometer (NICMOS) onboard the *Hubble Space Telescope*. Two data sets acquired with the NICMOS1 in the *F190N* filter on two distinct objects are used: the first target is a calibration star, SAO 179809, which was observed in 1998; the second is the high-proper motion star GJ 164, around which a companion was astrometrically discovered and whose existence was confirmed after point-spread function (PSF) modelization and subtraction of these NICMOS1 images by Pravdo et al. (2004). This latter target is an ideal benchmark: given its expected $<10:1$ luminosity contrast, one should expect a strong, unambiguous Ker-phase signal.

Moreover, ground-based infrared aperture masking interferometry measurements reported by Martinache et al. (2009) combined with the astrometry have led to strong constraints on the orbit of the companion around the primary. The location of GJ164 B measured from the Ker-phase analysis of the data can be compared to the orbit prediction.

Figure 2 shows the model of the pupil used for this exercise. The *HST* pupil exhibits a 30% central obscuration as well as 90° spider arms (actual dimensions were taken from the NICMOS1 configuration file in the TinyTim PSF simulation package for

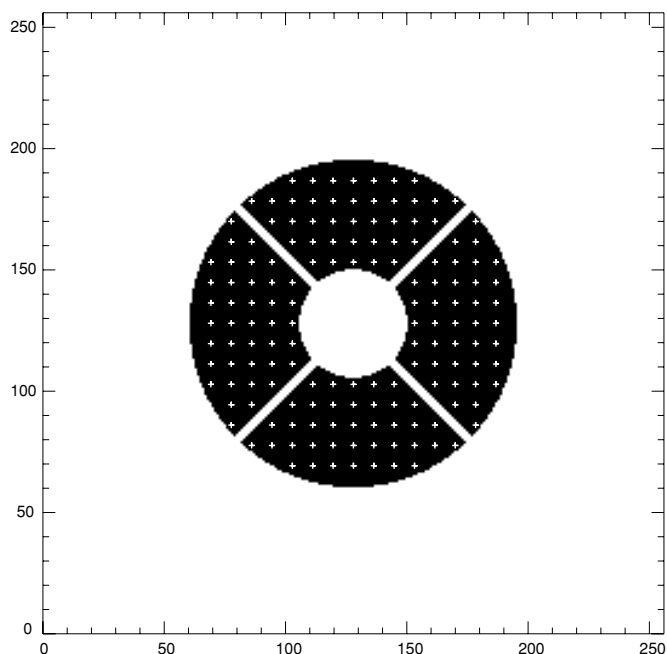


Figure 2. Model for the geometry of the *HST*/NICMOS pupil and location of the sample points for the determination of the Ker-phase relations. The 156 sample points of the pupil fall on a regular square grid with a step of $1/16$ of a pupil diameter that do not intersect with the central obstruction or the spider arms.

HST). The phase across the pupil is discretized into a 156 elementary sub-aperture array, whose locations fall on a regular square grid of step of $1/16$ of the outer pupil diameter. The phase sample is assembled into a 155-component ($N - 1$) vector φ .

These 156 pupil phase samples map in the (u, v) -plane onto a square grid of 366 distinct elements.² The resulting (u, v) -sampling is illustrated in Figure 3. For this analysis, \mathbf{A} (cf. Equation (1)) is therefore a 155×366 rectangular matrix, whose SVD reveals that 78 singular values are non-zero, leaving $366 - 78 = 288$ Ker-phase relations.

The GJ164 data consist of a total of 80 frames, acquired at average Julian Date 2453049.3 (2004 February 14 UT). Each image is a non-saturated 32 s exposure, and the target was acquired in a total of 10 distinct dither positions. Note that this

² Note for reference that a non-redundant array of 156 sub-apertures would produce exactly 12,090 distinct (u, v) points.

data set does not include images on a point source and therefore, the Ker-phases calculated from this data set are non-calibrated. Images corresponding to one dither position were simply co-added forming a final total of ten 250 s exposure images, and assembled into a data cube. The SAO 179809 data consist of four distinct 20 s exposure frames assembled into a separate data cube.

For both data cubes, the images were then centered with sub-pixel accuracy and windowed by a super-Gaussian function as described by Kraus et al. (2008) to limit sensitivity to readout noise. The window size is about $25\lambda/D$ in diameter, which is significantly larger than the field of view in which this technique is relevant.

After this preparatory stage, the images are simply Fourier-transformed (cf. second panel of Figure 3), and the signal $\mathbf{R} \cdot \Phi$ is directly measured for each of the 366 (u, v) points by sampling the imaginary part of the local complex visibility. The uncertainty associated with the measurement of each phase is estimated from the dispersion of the signal in the direct neighborhood of the (u, v) point.

The (u, v) signals are then assembled into Ker-phases using the relations gathered in the rows of \mathbf{K} and uncertainties are propagated. The procedure is repeated for each of the frames within each data cube. The final retained series of 288 Ker-phases is the weighted average for all frames.

Because the Ker-phase relations are designed to produce quantities independent from pupil phase errors, a point source is expected to exhibit zero signal within uncertainty. Despite the small number of statistics (four frames acquired on SAO 179809), the Ker-phase of the calibrator do average to zero (with a 19.7° standard deviation), while the binary exhibits a large signal amplitude ($>100^\circ$) in comparison with the uncertainty of individual Ker-phases ($\sim 2^\circ$). The third panel of Figure 3 compares the Ker-phase histograms of both data sets.

To further investigate the GJ 164 data, a parametric model of the (u, v) -plane phase Φ_O for a binary star is needed. The parameters are the angular separation, the position angle of the secondary relative to the primary, and the luminosity contrast ratio. The model phase Φ_O is then multiplied by the diagonal matrix \mathbf{R} , and finally, transformed into model Ker-phases using the relations established during the SVD.

The agreement between the data and the model is very good (cf. panel 4 of Figure 3), considering the large number of measurements (288) adjusted by only three parameters. The uncertainties on the Ker-phases, determined from the scatter of

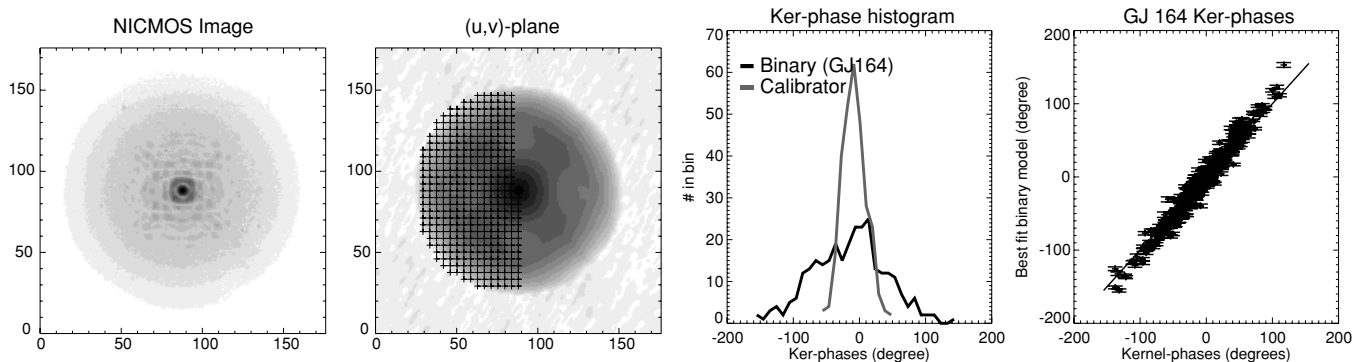


Figure 3. From left to right: example of a narrowband ($F190N$) NICMOS1 image used for this work, visualized with a nonlinear brightness scale; the Fourier transform of this image. The 366 sample points for the phase in the Fourier domain are overlaid; a comparison of histograms of the 288 Ker-phases calculated using the relations identified in Section 2.1. By design, the Ker-phases calculated from images of a single star are expected to be zero within uncertainty: the corresponding histogram (gray curve) confirms this expectation. In comparison, the Ker-phase histogram of the binary (dark curve) appears significantly larger. The same GJ164 Ker-phases plotted against the model of a binary star that best fits the data convince of the presence of a companion in the data.

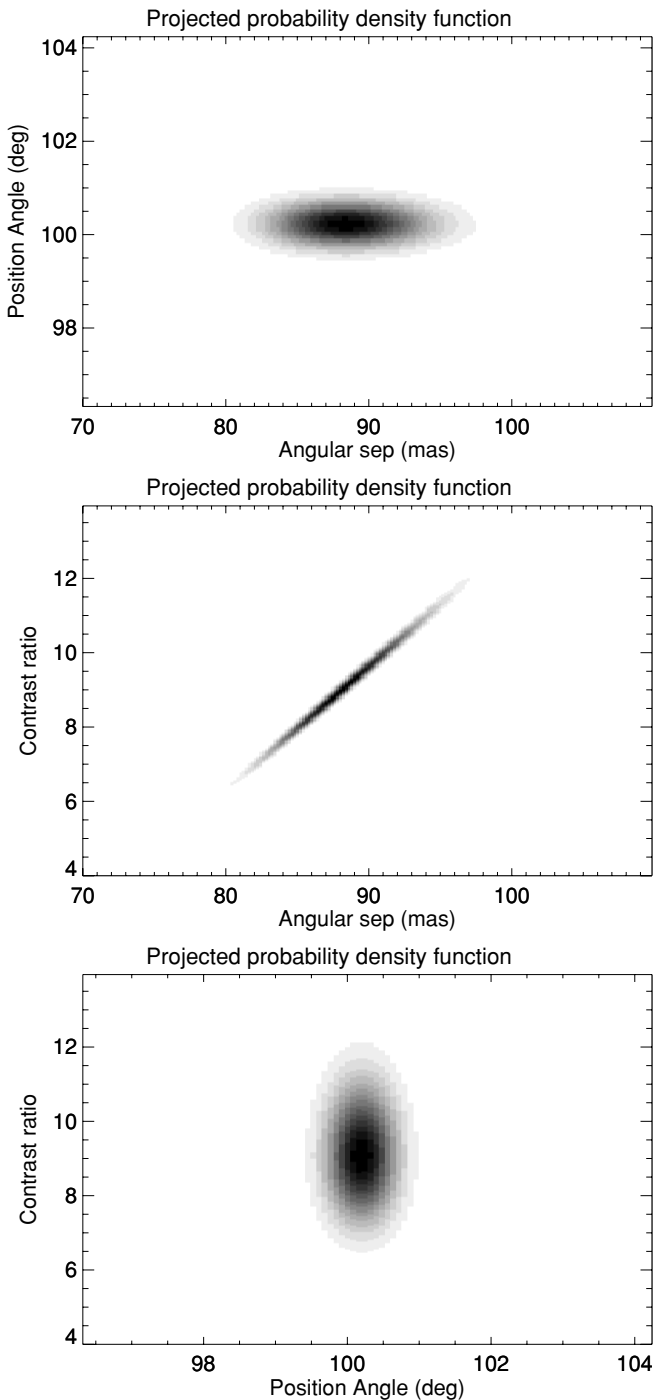


Figure 4. To determine confidence intervals for the parameters of the binary, a likelihood analysis comparable to the one presented by for closure phase was performed. These panels show the three projections of the likelihood function in the region of best fit. Except for the expected correlation between angular separation and contrast ratio for a detection within $1 \lambda/D$, the solution is unambiguous and well constrained, demonstrating the elegance of the Ker-phase approach.

the data however, lead to a best-fit reduced χ^2 larger than 1. A global error term (10°) is then added in quadrature to the uncertainty to account for a systematic error in the non-calibrated Ker-phase and produce a final reduced $\chi^2 = 1$.

One can then proceed with determining the uncertainty on the parameters of the model fit, by close examination of the likelihood function, very much like what is described in Martinache et al. (2009). The three panels of Figure 4 show the

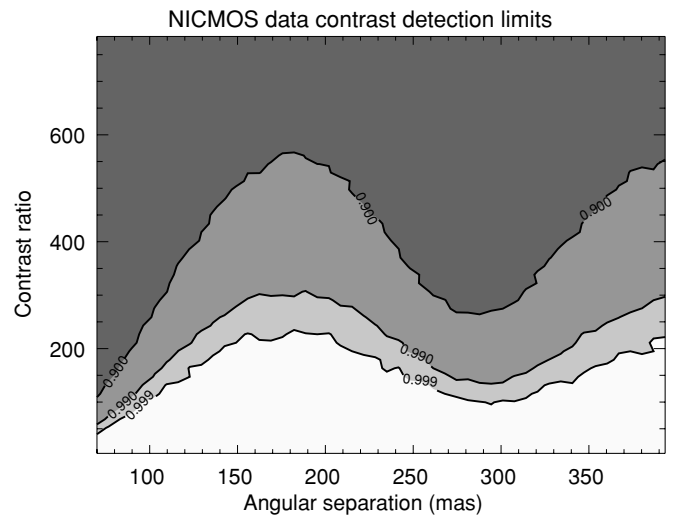


Figure 5. Level of confidence in the detection of a companion from the analysis of the *HST*/NICMOS data with the Ker-phase algorithm. A darker color indicates a region of lower confidence level. Three levels are highlighted: the 90%, 99%, and 99.9% confidence levels. At angular separation $0.5 \lambda/D$ (i.e., 80 mas at $\lambda = 1.9 \mu\text{m}$), a contrast limit better than 50:1 is possible at the 99% confidence level.

Table 1
Ker-Phase Detection of GJ164B in Nicmos Data Compared to Prediction from Orbital Parameters

Parameter	Ker-phase fit	Prediction
Separation (mas)	88.5 ± 3.6	88.2
P.A. (deg)	100.6 ± 0.3	100.4
Contrast	9.1 ± 1.2	

evolution of this function in the parameter space region near the best solution. Just like with closure phase data, at angular separations less than $1 \lambda/D$, contrast and separation appear to be correlated.

The uncertainty on each parameter of the model fit is determined after marginalization of the likelihood function over the other two parameters. Despite the noted correlation, the constraint on the parameters appears satisfactory, and the best fit (cf. Table 1) lies well within 1σ of the position predicted from the orbital parameters determined from NRM interferometry from the ground. It also matches the location reported by Pravdo et al. (2004), after subtraction of a simulated PSF from the same data, only with a constraint on the position angle improved by a factor of 10.

From its $(H - K)$ color index, Martinache et al. (2009) were able to conclude that GJ 164 B is of spectral type later than M8.5, while the primary is well characterized as an M4.5 dwarf. One of the most prominent spectral features for M dwarfs is the broad absorption band of water at $1.8 \mu\text{m}$, getting deeper with later types (Jones et al. 1994; Leggett et al. 2001). The $\sim 5:1$ contrast ratio quoted in the NRM paper was determined over the full K_s filter (bandwidth $2.0\text{--}2.3 \mu\text{m}$). A careful examination of the spectral sequence by (Jones et al. 1994) reveals that for this combination of spectral types, the luminosity of GJ 164B relative to GJ164A seen in the NICMOS F190N filter is expected to drop by 30%–40% due to the water absorption band. The 9:1 contrast determined from the Ker-phase model (cf. Table 1) in this narrow filter reflects this evolution. The analysis of this GJ164 data demonstrates the validity of the Ker-phase approach, by positively detecting a companion whose existence was known beforehand. This $<10:1$ contrast detection was how-

ever expected to be easy, despite the small angular separation of the detection ($0.6 \lambda/D$).

Typical NICMOS1 data sets on a given target usually consist of four frames only. The SAO 179809 data set is then a representative example and the statistics of its Ker phase ($\sigma = 19:7$) can be used in a Monte Carlo simulation to determine contrast detection limits.

Because the sampling of the (u, v) -plane exhibits no gap, the sensitivity does not depend on the position angle relative to the central star. One can however expect it to be a function of angular separation. A total of 10,000 simulations were performed per point in the angular separation/contrast plane to produce the sensitivity map displayed in Figure 5. The map highlights the 90%, 99%, and 99.9 % confidence level detection thresholds.

The technique looks promising: for such a data set, at $0.5 \lambda/D$, a 50:1 contrast detection appears possible at the 99% confidence level. The sensitivity increases and peaks at 180 mas, which unsurprisingly corresponds to the location of the first zero of the diffraction for the centrally obstructed telescope (about $1.1 \lambda/D$), and reaches $\sim 200:1$.

4. CONCLUSION

Classical closure phase appears to be one special case of a wider family of observable quantities that are immune to phase noise and non-common path errors. In the high-Strehl regime, it was demonstrated that closure phase like quantities, called Ker-phases, can be extracted from focal plane images, and provide high-quality “interferometric grade” information on a source, even when the pupil is redundant. The Ker-phase technique was successfully applied to a series of archive NICMOS images, clearly detecting a 10:1 contrast companion at a separation of $0.5\lambda/D$. Non-calibrated Ker-phase appears sensitive to the presence of 200:1 contrast companion at angular separation $1\lambda/D$. Re-analysis of other comparable NICMOS data sets with this technique might very well lead to the detection of previously undetected objects in the direct neighborhood of nearby stars.

Unlike closure phases, which are extremely robust to large wavefront errors, the use of Ker-phases is however for now restricted to the high-Strehl regime, and will only become relevant to ground-based observations when extreme AO systems become available. There is nevertheless hope to be able to extend the application of Ker-phases to not-so-well corrected AO images, using additional differential techniques. One possibility, consists in using integral field spectroscopy to follow in the Fourier plane the evolution of the complex visibilities as a function of wavelength. With enough resolution and spectral coverage, this indeed allows us to identify the phasors contributing to the power contained at one spatial frequency.

The SVD of the transfer matrix used to create Ker-phase relations can also be used to produce a pseudoinverse to the matrix, and in some cases, allows us to invert the relation linking the (u, v) phases to the pupil phases. This means that under certain conditions, a single monochromatic focal plane image can also be useful for wavefront sensing purposes. This is particularly interesting since the measurement is happening at the level of the final science detector, which therefore allows us to calibrate non-common path errors. The application of the formalism to wavefront sensing will be the object of a future publication.

The author thanks Michael J. Ireland and Olivier Guyon for the useful discussions of the ideas presented in this work. This work was supported in part by the Jet Propulsion Laboratory under contract 1379504.

REFERENCES

- Baldwin, J. E., Haniff, C. A., Mackay, C. D., & Warner, P. J. 1986, *Nature*, **320**, 595
- Baldwin, J. E., et al. 1996, *A&A*, **306**, L13
- Haniff, C. A., Mackay, C. D., Titterton, D. J., Sivia, D., & Baldwin, J. E. 1987, *Nature*, **328**, 694
- Ireland, M. J., Kraus, A., Martinache, F., Lloyd, J. P., & Tuthill, P. G. 2008, *ApJ*, **678**, 463
- Jennison, R. C. 1958, *MNRAS*, **118**, 276
- Jones, H. R. A., Longmore, A. J., Jameson, R. F., & Mountain, C. M. 1994, *MNRAS*, **267**, 413
- Kloppenborg, B., et al. 2010, *Nature*, **464**, 870
- Kraus, A. L., Ireland, M. J., Martinache, F., & Lloyd, J. P. 2008, *ApJ*, **679**, 762
- Labeyrie, A. 1996, *A&AS*, **118**, 517
- Labeyrie, A., Le Coroller, H., & Dejonghe, J. 2008, *Proc. SPIE*, **7013**, 107
- Leggett, S. K., Allard, F., Geballe, T. R., Hauschildt, P. H., & Schweitzer, A. 2001, *ApJ*, **548**, 908
- Lloyd, J. P., Martinache, F., Ireland, M. J., Monnier, J. D., Pravdo, S. H., Shaklan, S. B., & Tuthill, P. G. 2006, *ApJ*, **650**, L131
- Martinache, F., Lloyd, J. P., Ireland, M. J., Yamada, R. S., & Tuthill, P. G. 2007, *ApJ*, **661**, 496
- Martinache, F., Rojas-Ayala, B., Ireland, M. J., Lloyd, J. P., & Tuthill, P. G. 2009, *ApJ*, **695**, 1183
- Monnier, J. D. 2000, in *Principles of Long Baseline Stellar Interferometry*, ed. P. R. Lawson (Pasadena, CA: NASA), 203
- Monnier, J. D., et al. 2007, *Science*, **317**, 342
- Pravdo, S. H., Shaklan, S. B., Henry, T., & Benedict, G. F. 2004, *ApJ*, **617**, 1323
- Press, W. H., Teukolsky, S. A., Vetterling, W. T., & Flannery, B. P. 2002, *Numerical recipes in C: The Art of Scientific Computing* (2nd ed.; New York: Cambridge Univ. Press)
- Rajagopal, J. K., Barry, R., Lopez, B., Danchi, W. C., Monnier, J. D., Tuthill, P. G., & Townes, C. H. 2004, *Proc. SPIE*, **5491**, 1120
- Readhead, A. C. S., Nakajima, T. S., Pearson, T. J., Neugebauer, G., Oke, J. B., & Sargent, W. L. W. 1988, *AJ*, **95**, 1278
- Sivaramakrishnan, A., et al. 2009, *Proc. SPIE*, **7440**, 30
- Tuthill, P. G., Monnier, J. D., Danchi, W. C., Wishnow, E. H., & Haniff, C. A. 2000, *PASP*, **112**, 555
- Tuthill, P. G., et al. 2006, *Proc. SPIE*, **6272**, 103